

PEARLS: Discovery of Point-Source Features Within Galaxies in the North Ecliptic Pole Time Domain Field

RAFAEL ORTIZ III,¹ ROGIER A. WINDHORST,¹ SETH H. COHEN,¹ STEVEN P. WILLNER,² ROLF A. JANSEN,¹ TIMOTHY CARLETON,¹ PATRICK S. KAMIENESKI,¹ MICHAEL J. RUTKOWSKI,³ BRENT M. SMITH,¹ JAKE SUMMERS,¹ CHENG CHENG,⁴ DAN COE,⁵ CHRISTOPHER J. CONSELICE,⁶ JOSE M. DIEGO,⁷ SIMON P. DRIVER,⁸ JORDAN C. J. D'SILVA,^{8,9} BRENDA L. FRYE,¹⁰ HANSUNG B. GIM,¹¹ NORMAN A. GROGIN,¹² HEIDI B. HAMMEL,¹³ NIMISH P. HATHI,¹⁴ BENNE W. HOLWERDA,¹⁵ MINHEE HYUN,¹⁶ MYUNGSHIN IM,¹⁷ WILLIAM C. KEEL,¹⁸ ANTON M. KOEKEMOER,¹² JUNO LI,^{8,9} MADELINE A. MARSHALL,^{19,9} TYLER J. McCABE,¹ NOAH J. MCLEOD,¹ STEFANIE N. MILAM,²⁰ ROSALIA O'BRIEN,¹ NOR PIRZKAL,¹² AARON S. G. ROBOTHAM,⁸ RUSSELL E. RYAN, JR.,¹² CHRISTOPHER N. A. WILLMER,¹⁰ HAOJING YAN,²¹ MIN S. YUN,²² AND ADI ZITRIN²³

¹School of Earth and Space Exploration, Arizona State University, Tempe, AZ 85287-1404, USA

²Center for Astrophysics | Harvard & Smithsonian, 60 Garden St., Cambridge, MA 02138 USA

³Department of Physics and Astronomy, Minnesota State University, Mankato, MN 56001, USA

⁴Chinese Academy of Sciences South America Center for Astronomy, National Astronomical Observatories, CAS, Beijing 100101, China

⁵AURA for the European Space Agency (ESA), Space Telescope Science Institute, 3700 San Martin Drive, Baltimore, MD 21210, USA

⁶Jodrell Bank Centre for Astrophysics, Alan Turing Building, University of Manchester, Oxford Road, Manchester M13 9PL, UK

⁷Instituto de Física de Cantabria (CSIC-UC). Avda. Los Castros s/n. 39005 Santander, Spain

⁸International Centre for Radio Astronomy Research (ICRAR) and the International Space Centre (ISC), The University of Western Australia, M468, 35 Stirling Highway, Crawley, WA 6009, Australia

⁹ARC Centre of Excellence for All Sky Astrophysics in 3 Dimensions (ASTRO 3D), Australia

¹⁰Steward Observatory, University of Arizona, 933 N Cherry Ave, Tucson, AZ, 85721-0009, USA

¹¹Department of Physics, Montana State University, Bozeman, MT 59717, US

¹²Space Telescope Science Institute, 3700 San Martin Drive, Baltimore, MD 21210, USA

¹³Association of Universities for Research in Astronomy, Washington, D.C. 20004, USA

¹⁴Space Telescope Science Institute, 3700 San Martin Drive, Baltimore, MD 21218, USA.

¹⁵Department of Physics, University of Louisville, Natural Science Building 102, Louisville KY 40292, USA

¹⁶Korea Astronomy and Space Science Institute, Yuseong-gu, Daejeon 34055, Republic of Korea

¹⁷SNU Astronomy Research Center, Dept. of Physics & Astronomy, Seoul 08826, Republic of Korea

¹⁸Department of Physics and Astronomy, University of Alabama, Box 870324, Tuscaloosa, AL 35404, USA

¹⁹National Research Council of Canada, Herzberg Astronomy & Astrophysics Research Centre, 5071 West Saanich Road, Victoria, BC V9E 2E7, Canada

²⁰Astrochemistry Laboratory, NASA Goddard Space Flight Center, Greenbelt, MD 20771, USA

²¹Department of Physics and Astronomy, University of Missouri, Columbia, MO 65211, USA

²²Department of Astronomy, University of Massachusetts, Amherst, MA 01003, USA

²³Department of Physics, Ben-Gurion University of the Negev, P.O. Box 653, Be'er-Sheva 84105, Israel

ABSTRACT

The first public 0.9–4.4 μm NIRCam images of the North Ecliptic Pole (NEP) Time Domain Field (TDF) uncovered galaxies displaying point-source features in their cores as seen in the longer wavelength filters. We visually identified a sample of 66 galaxies (~ 1 galaxy per arcmin²) with point-like cores and have modeled their two-dimensional light profiles with `GalFit`, identifying 16 galactic nuclei with measurable point-source components. `GalFit` suggests the visual sample is a mix of both compact stellar bulge and point-source galaxy cores. This core classification is complemented by spectral energy distribution (SED) modeling to infer the sample's active galactic nucleus (AGN) and host-galaxy parameters. For galaxies with measurable point-source components, the median fractional AGN contribution to their 0.1–30.0 μm flux is 0.44, and 14/16 are color-classified AGN. We conclude that near-infrared point-source galaxy cores are signatures of AGN. In addition, we define an automated sample-selection criterion to identify these point-source features. These criteria can be used in other extant and future NIRCam images to streamline the search for galaxies with unresolved IR-luminous AGN. The James Webb Space Telescope's superb angular resolution and sensitivity at infrared wavelengths is resurrecting the morphological identification of AGN.

Keywords: Active Galactic Nuclei(16) — Seyfert Galaxies(1447) — James Webb Space Telescope(2291) — Spectral Energy Distribution(2129)

1. INTRODUCTION

More than eighty years ago, Carl [Seyfert](#) (1943) drew attention to 6 “extragalactic nebulae” with broad emission lines and “exceedingly luminous stellar or semistar” nuclei. Galaxies of this type became known as “Seyfert galaxies” ([Burbidge et al. 1963](#)), and they are now recognized (e.g., [Osterbrock 1993](#)) as members of the low-luminosity end of the population of active galactic nuclei (AGN).

AGN are now thought to consist of an accretion disk around a supermassive black hole (SMBH) within a wider, optically thick dust torus (e.g., [Antonucci & Miller 1985](#)). This central engine can emit enormous luminosities and can even outshine the entire host galaxy (e.g., [Padovani et al. 2017](#)). Modern studies of AGN probe the relationship with their host galaxies and intergalactic environments along with properties of the central SMBHs (e.g., [Bollati et al. 2023](#); [Costa-Souza et al. 2023](#); [Sampaio et al. 2023](#)).

AGN emit energy across the entire electromagnetic spectrum, and identification and classifications of AGN are based on X-ray (e.g., [Elvis et al. 1978](#)), UV-visible (e.g., [Seyfert 1943](#)), infrared (e.g., [Stern et al. 2005](#)), and radio (e.g., [Fanaroff & Riley 1974](#)) observations. AGN are most often identified via their spectral energy distributions (SED)s (e.g., [Li et al. 2023](#); [Lyu et al. 2023](#); [Yang et al. 2023](#)), their colors (e.g., [Stern et al. 2005](#); [Hwang et al. 2021](#); [Juodžbalis et al. 2023](#); [Furtak et al. 2023](#)), spectroscopy (e.g., [Mehdipour et al. 2024](#); [Burke et al. 2024](#)), variability (e.g., [Pouliasis et al. 2019](#); [O’Brien et al. 2024](#)), radio (e.g., [Hyun et al. 2023](#)), or X-ray emission (e.g., [Masini et al. 2020](#); [Zhao et al. 2021](#)). However, heavily obscured AGN whose intrinsic UV-visible signatures are hidden by dust may be missed (e.g., [Glikman et al. 2012](#); [Hickox & Alexander 2018](#)), and at infrared wavelengths, where the dust extinction is lower, wide-field surveys can only be done from space. Until now, the low angular resolution of infrared space observatories and the “big data” era of advanced instrumentation and vast surveys (such as the Sloan Digital Sky Survey ([York et al. 2000](#))) has caused identification of AGN through visual morphologies to have fallen out of favor.

Recent work indicates that a significant population of redder AGN exists. Their UV-visible SEDs suggest intermediate levels of extinction, $A_V \sim 1\text{--}3$ mag (e.g., [Wilkes et al. 2002](#); [Richards et al. 2003](#); [Trump et al. 2013](#); [Cales & Brotherton 2015](#); [Wang et al. 2019](#)). These objects exhibit hybrid properties, blurring the lines between canonical AGN classifications, and may represent an important evolutionary phase. For instance, modeling suggests the AGN torus geometry evolves as material accretes onto the black hole (e.g.,

[Ohsuga & Umemura 2001](#); [Mandal et al. 2018](#)), with early dust-free to intermediate-stage reddened phases necessarily preceding the well-studied mature dust-obscured AGN. Disentangling the nature of these moderately-reddened AGN exhibiting a blend of obscured and unobscured traits has proved challenging but vitally important for refining our understanding of the complex coevolution between SMBHs and their host galaxies over cosmic time. Detailed multi-wavelength modeling is critical to robustly characterize the properties of these objects.

The James Webb Space Telescope (JWST), with its unprecedented resolution in the infrared (e.g., [Davies et al. 2024](#); [Li et al. 2023](#); [Yang et al. 2023](#)), offers the chance to revisit morphological selection and analysis of AGN. This paper is an initial exploration of the possibilities via the characteristic diffraction spikes of JWST’s point-spread function (PSF) at the longer near-infrared wavelengths that suggest pointlike galaxy cores.

The North Ecliptic Pole (NEP) Time Domain Field (TDF; [Jansen & Windhorst 2018](#)) is located within JWST’s continuous viewing zone, making it a prime target for AGN variability and other time-domain science. Because the ultimate goal will be to compare morphological selection with other methods, we used the now-public JWST NEP-TDF images ([Windhorst et al. 2023](#)) to visually search for galaxies with point-like features in their center, i.e., potential AGN, following the core morphology and Seyfert class relationship (e.g., [Windhorst & Cohen 2010](#); [Rutkowski et al. 2013](#)). The morphologically selected sample was then analyzed in order to infer physical parameters and AGN presence.

Section 2 describes the observations and data, along with the construction of a morphologically selected AGN catalog and a means to automate the selection of galaxies with point-source nuclei. Section 3 discusses the results of fitting 2D-light profiles and various galaxy SEDs to the sample, and Section 4 gives a summary. All magnitudes are in AB units ([Oke & Gunn 1983](#)). Where relevant, we adopt a flat Λ CDM cosmology with $H_0 = 68 \text{ km s}^{-1} \text{ Mpc}^{-1}$, $\Omega_M = 0.32$, and $\Omega_\Lambda = 0.68$ ([Planck Collaboration et al. 2016, 2020](#)).

2. DATA & CATALOGING

2.1. Observations

The JWST NEP-TDF is centered at (RA, Decl.)_{J2000} = (17:22:47.896, +65:49:21.54) ([Jansen & Windhorst 2018](#)). The TDF was observed with JWST as part of the Prime Extragalactic Areas for Reionization and Lensing Science (PEARLS) GTO program ([Windhorst et al. 2023](#)) in eight NIRCam filters: F090W, F115W, F150W, F200W, F277W,

F356W, F410M, and F444W. The observations consisted of four orthogonal spokes (see Figure 1 of O’Brien et al. 2024) observed between 2022 Aug 25 and 2023 May 30. The NIRCam image quality is diffraction-limited at wavelengths $\gtrsim 1.3 \mu\text{m}$ (Rigby et al. 2023; Windhorst et al. 2023) with point source FWHM values ranging from 60–160 milliarcseconds (mas) at wavelengths of 1.3–4.8 μm .

The data were retrieved from MAST and post-processed by the PEARLS team using their custom pipeline to mitigate $1/f$ -noise, identify and subtract wisps in the NIRCam/SW filters, mask snowball artifacts, and flatten the background across read-out amplifier boundaries. The individual post-processed images were rectified and aligned to Gaia/DR3. Full mosaics of the field were created for each filter with a 0''.030 pixel scale. The 5σ point-source limit is typically between 28.0 and 29.1 mag, depending on the filter, and 29.0 mag in F200W specifically. Windhorst et al. (2023), Robotham et al. (2023), and Jansen et al. 2024a (in prep.) give more details of the data reduction, calibration, and post-processing.

While the primary focus of this work is the ability to identify and analyze likely AGN with JWST/NIRCam photometry, we incorporate ancillary *HST* observations of the NEP-TDF with the Wide Field Camera 3 (WFC3/UVIS) in the F275W filter ($\lambda_c \simeq 0.272 \mu\text{m}$) and with the Advanced Camera for Surveys (ACS/WFC) in the F435W and F606W filters ($\lambda_c \simeq 0.433$ and $0.592 \mu\text{m}$, respectively) with a total area of $\simeq 194 \text{ arcmin}^2$ (ACS/WFC). Observations from *HST* GO 15278 were taken between 2017 October 1 and 2019 February 9 and those from GO 16252+16793 (TREASURE-HUNT) between 2020 September 25 and 2022 October 31. Both programs used 4-orbit CVZ visits to reach 2σ limiting depths of $m_{\text{AB}} \simeq 28.0, 28.6$, and 29.5 mag in F275W, F435W and F606W, respectively. O’Brien et al. (2024, §2.1) and Jansen et al. (2024b; in prep.) give further details of the *HST* observations.

For an initial comparison with longer-wavelength observations in the NEP-TDF, we used the VLA 3 GHz radio observations detailed by Hyun et al. (2023, their Appendix A).

2.2. Catalogs & Samples

We used SExtractor (Bertin & Arnouts 1996) to generate catalogs. The detection threshold required 9 contiguous pixels 1.5σ above the background. We used 32 deblending sub-thresholds with a 0.06 minimum contrast necessary for object deblending. We ran SExtractor on all eight filters in dual-image mode using F444W as the detection filter to produce position-matched catalogs of the entire JWST NEP-TDF. Magnitudes are MAG_AUTO except where indicated otherwise.

We position-matched objects in both right ascension and declination between *HST* (O’Brien et al. 2024) and VLA

(Hyun et al. 2023) catalogs using 0''.1 and 0''.5 separations, respectively, to identify counterparts to the samples used in our analysis.

We used both the EAZY¹ (Brammer et al. 2008) and CIGALE² (Boquien et al. 2019) SED-fitting codes to compute photometric redshifts for our samples, as discussed in Section 3. We used the CIGALE-computed photometric redshifts for nominal redshifts in this work and for sample construction because the CIGALE fitting incorporates multiple components, including AGN, whereas EAZY was tuned for single-template fitting.

2.3. Visual Sample Selection

ROIII visually inspected an 8-filter color-composite of all NIRCam observations within the JWST NEP-TDF to identify resolved galaxies with unresolved point-like features in their cores. The color-composite was constructed according to the Trilogy³ prescription (Coe et al. 2012). The entire JWST NEP-TDF was visually inspected for galaxies that displayed the characteristic diffraction spikes or PSF effects from compact, luminous galaxy cores. This identified 66 galaxies⁴, which we refer as “CPGs” (central point-source galaxies) hereafter. Table 1 lists the CPGs, and Figure 1 shows their images and highlights the qualitative criteria, diversity, and similarities of the CPGs. Several objects within the CPG sample display obvious point-like features in their cores (i.e., IDs 1, 14, 28, 48), whereas the vast majority show less distinct features of the characteristic PSF from JWST.

The NIRCam images of the NEP-TDF sampled an area of 65.4 arcmin^2 , and hence our sample of 66 CPGs corresponds to ~ 1 galaxy per arcmin^2 to $m_{\text{F444W}} \lesssim 22 \text{ AB mag}$. This is comparable to the WISE ($W_1 - W_2$) color-selected AGN density (e.g., Assef et al. 2013, their Table 1), $\sim 0.5 \text{ AGN per } \text{arcmin}^2$ to $m_{W_2} \lesssim 20.5 \text{ AB mag}$.

2.4. Automated Sample Selection

While our initial sample was obtained through qualitative visual selection, a quantitative method is needed to identify objects similar to CPGs, especially for large surveys. The concentration index (e.g., Conselice 2003) is one measure, but its basic ratio finds sources that are peaky but not necessarily pointlike. Instead, we used SExtractor to measure F444W magnitudes in circular apertures at the object cores. Aperture radii were 6, 8, and 10 pixels, corresponding to radii 0''.18, 0''.24, and 0''.30, respectively. We adopted these aper-

¹ <https://github.com/gbrammer/eazy-photoz>

² <https://cigale.lam.fr/>

³ <https://www.stsci.edu/~dcoe/trilogy>

⁴ We verified that no objects in the sample are stars by applying a FWHM and magnitude cut similar to that used by Windhorst et al. (2023) and by requiring $z_{\text{phot}} \neq 0$.

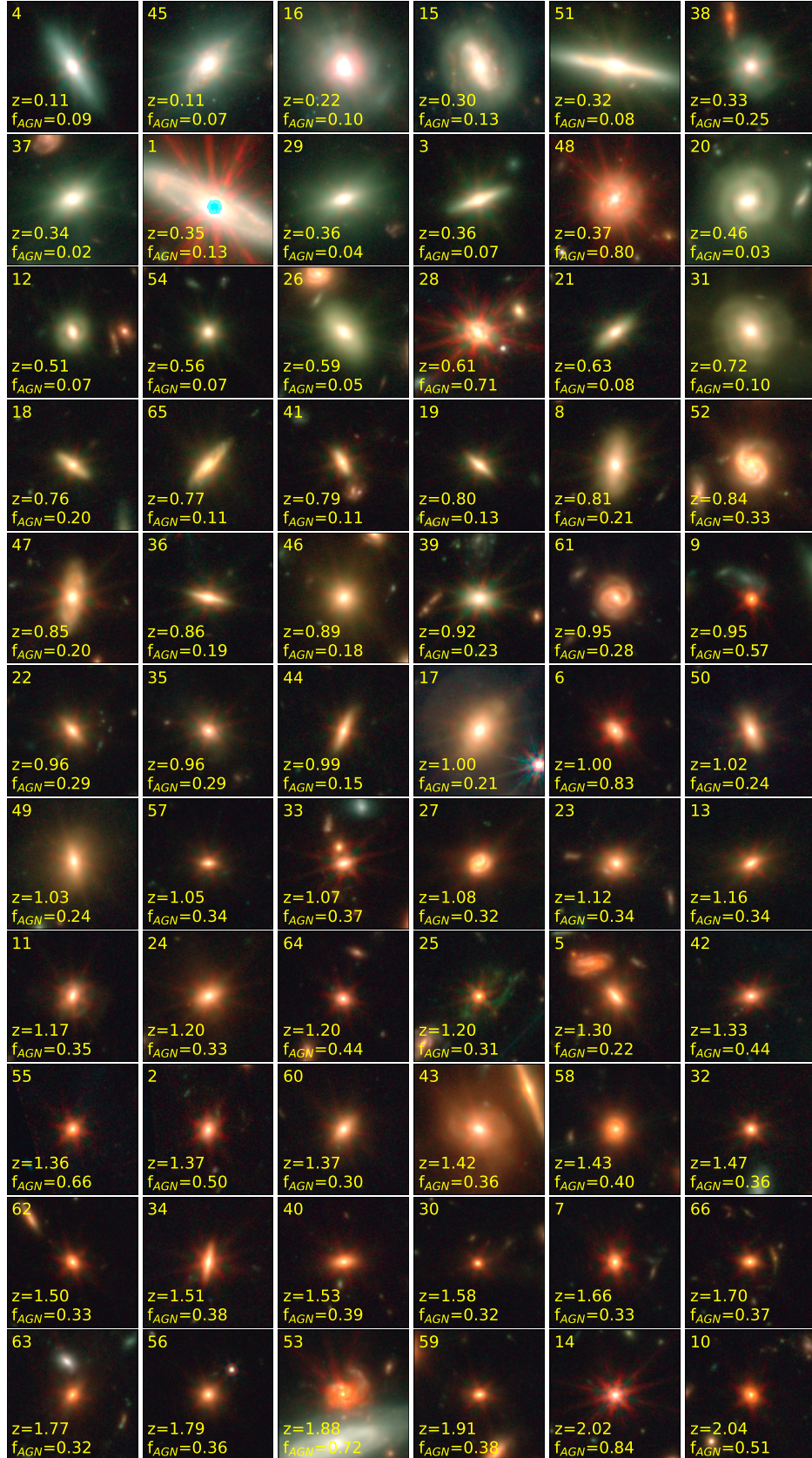


Figure 1. RGB image cutouts for the 66 CPGs sorted by z_{phot} from CIGALE. All image cutouts are $6''$ square. The top left corner of each image gives the image ID from Table 1, and z_{phot} and f_{AGN} are in the bottom left. The RGB scaling is R = 0.3·F356W + 0.8·F410M + 1.0·F444W, G = 1·F200W + 0.7·F277W + 0.5·F356W, B = 1·F090W + 1·F115W + 1·F200W + 1·F277W + 0.5·F356W + 0.5·F410M + 0.5·F444W.

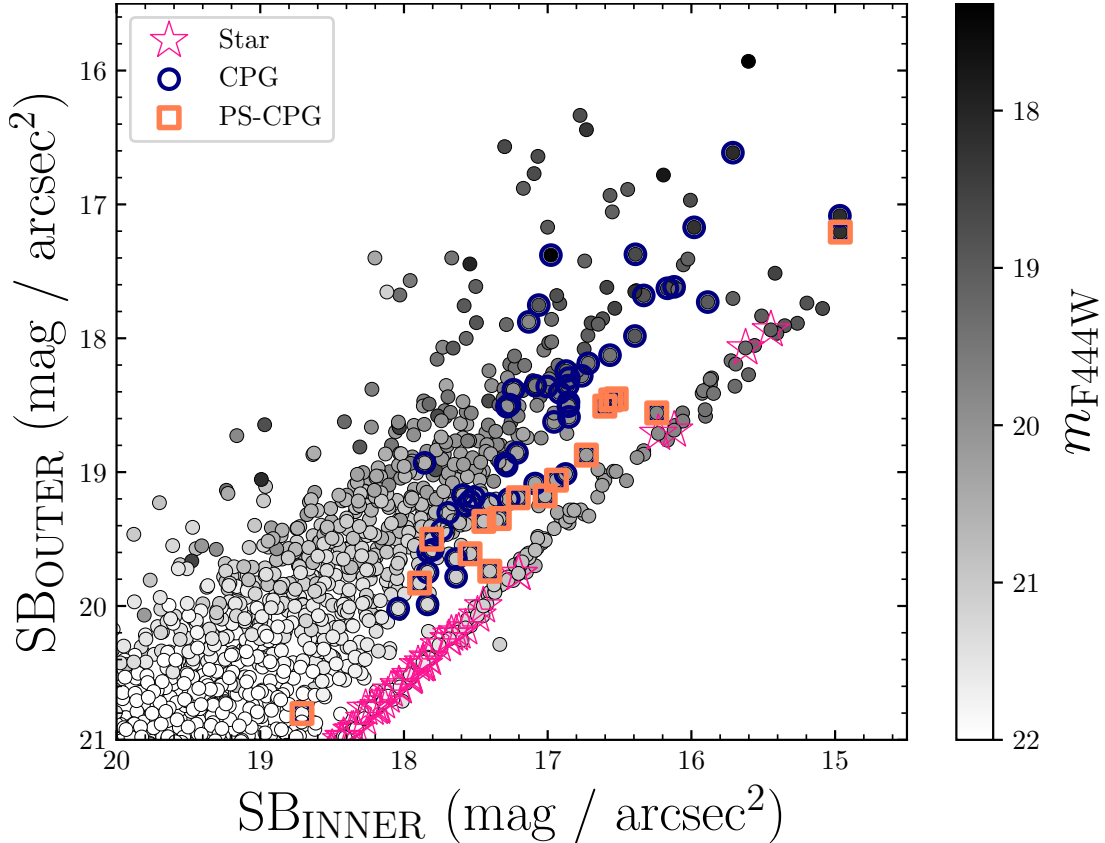


Figure 2. F444W central surface brightness versus the surface brightness in a surrounding annulus. The central surface brightness was measured in a circular aperture with a radius $0''.18$, and the outer annulus between circular apertures of $0''.24$ and $0''.36$. Navy blue circles and orange squares represent CPGs and Point-Source CPGs (see § 3.1), and pink stars represent stars in the field (Windhorst et al. 2023). Only objects with $m_{\text{F444W}} < 22$ AB mag, the limiting magnitude of the CPG sample, are plotted. The greyscale bar (right) maps the galaxy total F444W magnitudes (MAG_AUTO), with brighter galaxies plotted as darker.

tures to probe the surface brightness near the cores of the CPG sample and identify objects that are morphologically similar to stars out to a certain radius. We used the smallest aperture to measure the average surface brightness within an inner area of $\sim 0.1 \text{ arcsec}^2$ (SB_{INNER}) and used the two other apertures to measure the average surface brightness within an outer annulus (SB_{OUTER}), which has an area equal to that within the inner circular aperture. Multiple aperture radii for SB_{INNER} and SB_{OUTER} were tested, and by experiment the ones adopted provided the most effective way to probe point-source features in galaxies.

Figure 2 plots SB_{OUTER} against SB_{INNER}. Stars are identified as straddling the NIRCam diffraction limit with $150 \text{ mas} \leq \text{FWHM} \leq 170 \text{ mas}$ with $m_{\text{F444W}} \leq 28$ mag (Windhorst et al. 2023). CPGs near the stars in Figure 2 are Point-Source-CPGs (PS-CPGs), characterized and identified in §3.1 as having point-source cores. These objects show that there exists a parameter space where we can probe point sources within galaxies, barring contamination from other stars. The longer wavelengths of the near-infrared regime can probe both optically obscured and unobscured AGN (e.g., Assef et al. 2013) and both star-forming galaxies

and weak AGN (e.g., Kim et al. 2019) via redder colors in the $3.5\text{--}3.6 \mu\text{m}$ and $4.4\text{--}4.5 \mu\text{m}$ bands. Thus, JWST’s aperture photometry—in contrast to shorter wavelength data—can be more effective at probing morphological signatures of AGN at these wavelengths. Obscured AGN in the UV-visible are likely showing up in these images because of the much smaller dust extinction at these wavelengths, and we carried out complementary SED analysis (§ 3) to clarify whether AGN are the most probable explanation for the point-like features in our infrared CPGs.

The above classification procedure provides a robust star-CPG separation and a CPG separation from brighter galaxies that automatically recovers our CPG sample and finds objects similar to it. Particularly, this classification procedure can probe the presence of a point source within resolved galaxies. Identifying galaxies that straddle the morphology of stars (such as the orange squares in Figure 2 representing PS-CPGs) without contamination would allow a search for galaxies with point-like cores in any JWST/NIRCam image. The automated method does not pick up all of the weak Seyferts; some will require higher signal-to-noise data to be identified by this procedure.

2.5. Control Sample

Understanding how CPGs differ from other galaxies requires a comprehensive control sample. To create one, we find the four most similar galaxies in the *JWST* NEP-TDF with respect to brightness and CIGALE-computed photometric redshift down to AB mag ≤ 22 , the limiting magnitude for CPG selection. The resulting control sample has 225 galaxies, slightly fewer than $4 \times$ the CPG sample size. These are all the galaxies we could find with a similar m_{F444W} and photometric redshift distribution.

The control sample was also analyzed with the same two-dimensional light-profile and SED-analysis as the CPG sample, providing robust number statistics and similar galaxy demographics to assess the reliability of the classifications.

The first spoke of the NEP TDF, observed in 2022 Aug, had a scheduling interruption due to a guide star failure. The second half of that spoke was observed 10 days later, resulting in two sets of diffraction spikes rotated by 10° . The PSF structure with 12 diffraction spikes could not be modeled for morphological parameters with affordable computational efficiency, and that left only 132 control galaxies that could be so modeled. All other parameters were determined for the full control sample of 225 galaxies.

3. RESULTS & DISCUSSION

3.1. Two-Dimensional Light Modeling

We used the two-dimensional fitting algorithm *GalFit* (Peng et al. 2002) to model the $4.4 \mu\text{m}$ light profiles of the CPGs. We modeled all galaxies with both a double-Sérsic model and a Sérsic component plus a PSF component. Comparison of the two models determines whether CPGs contain true point sources or a compact stellar bulge. Many galaxies in both the CPG and control samples cannot be completely modeled with only two components, but this modeling approach is adequate to characterize the apparent point-like features. This structural analysis is primarily sensitive to AGN that have similar or higher luminosities to or higher than that of a central bulge.

The Sérsic profile is a robust representation of a variety of galaxy types because of its flexibility in profile characteristics. The Sérsic profile is parameterized as

$$I(R) = I_e \exp \left\{ -b_n \left[\left(\frac{R_m}{R_e} \right)^{1/n} - 1 \right] \right\}, \quad (1)$$

where I_e is the surface brightness at the half-light radius R_e , n is the Sérsic index, b_n is a derived parameter ensuring proper integration at R_e (and is the value at which the Gamma probability distribution function integrates to 0.5 with a shape parameter of $2n$), and R_m is the two-dimensional modified radius where the profile is being evaluated (e.g., Robotham et al. 2017). For our purposes, the

Sérsic profile is assumed to generally model the nucleus and extended stellar disc of a galaxy in a double-Sérsic component fit. For two-component fits with a Sérsic component and a PSF component, the Sérsic profile generally models the bulk of the extended galaxy, while the PSF component models an unresolved point source in the galaxy nucleus. Thus a *GalFit* analysis classifies the core type of the CPGs.

For both our CPG and control sample, we used a simulated $4.4 \mu\text{m}$ PSF from *WebbPSF* (Perrin et al. 2012) based on 300×300 pixel ($9'' \times 9''$) image stamps of each galaxy. We masked out neighboring objects through a *Extractor*-generated segmentation map and estimated the sky background using the uncertainty image from the *JWST* pipeline. A note at the end of Table 1 gives the constraints on the *GalFit* parameters. Figure 3 visualizes *GalFit* output for six CPGs.

Figure 4 compares the goodness-of-fit results for the single- and double-Sérsic fits. Most CPGs prefer the double-Sérsic fit, but 16 are best fit with the single-Sérsic component plus a PSF component. This is not the case for the control-sample galaxies. Many galaxies in both samples are equally well fit by both models with a preference for a double-Sérsic fit in borderline cases. The preference is consistent with the double-Sérsic having more free parameters. Both the CPG and control sample demonstrate a similar bulge-core frequency. Hereafter, we refer to CPGs with a point-source core classification from this two-component *GalFit* procedure as “PS-CPGs”, borderline cases as Undetermined-CPGs (“U-CPGs”), and bulge core classified CPGs are referred to as Bulge-CPGs (“Bulge”). This distinction is particularly useful when using SED techniques to infer physical properties of the CPGs with likely point-source features in their cores.

A number of CPGs are not completely fit with two-components. There are definitely galaxies within our CPG sample that were visually selected simply for having ultraluminous, compact nuclei, thus having steep Sérsic indices and showing faint features of the PSF. Consequently, these Bulge-CPGs are likely galaxies not hosting an observable AGN at our observed wavelengths and are more suggestive of being a compact stellar bulge or nuclear starburst (e.g., Bruce et al. 2016). It is reasonable to expect that the CPG sample would show a mix of true point-source and stellar-bulge cores. More comprehensive *GalFit* modeling would clarify the point-source presence in galaxies that are not well fit with only two components (i.e., U-CPGs). Nevertheless, Figure 4 suggests that the CPG sample does indeed have point-sources within galactic nuclei. Additional constraints from SED fitting are needed to clarify whether an AGN is responsible for these features.

3.2. Seyfert Template Fitting with EAZY

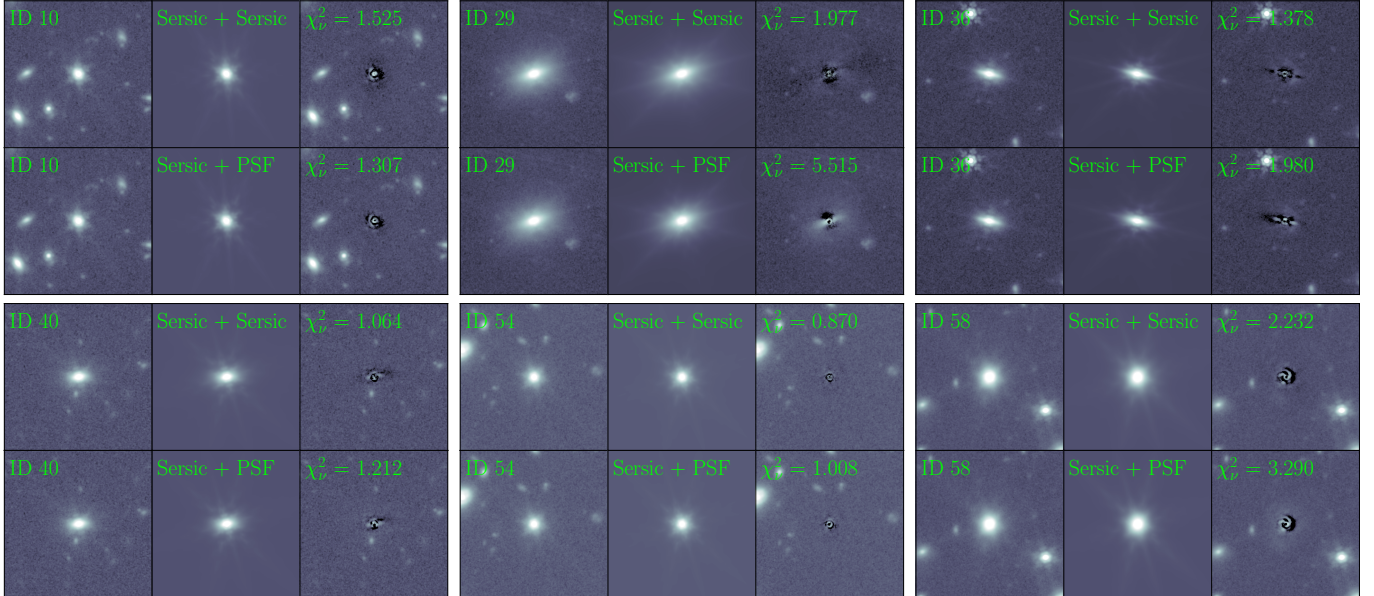


Figure 3. GalFit image output for six CPGs. For each object, there are six subpanels; the top three subpanels visualize the Sérsic+Sérsic fit, and the bottom three visualize the Sérsic+PSF fit. Each row shows the image (left), model (middle), and residual image (right). Green text identifies the CPG ID, the two-component fit, and the goodness of fit statistic, χ^2_ν , for the fit. The color map indicates negative flux in black and positive flux in white.

In order to estimate AGN fractions and derive photometric redshifts, we used EAZY to fit the photometry for each of the CPG and control sample galaxies. For this single-

component template fitting procedure, we ran EAZY twice: one run allowing a single-component fit from the 12 EAZY `tweak_fspcs_QSF12_v3` templates and a second run fitting the AGN-ATLAS SEDs. The former templates are galaxy templates used for stellar population synthesis and the latter templates (Brown et al. 2019) are blends of AGN and host-galaxy SEDs covering 0.09–30.0 μm . The host/AGN ratios available are powers of two from 0.5 to 64 normalized at 0.6 μm .

As shown in Figure 5, 70% of the CPGs prefer an AGN-ATLAS template over a standard EAZY template. Generally, the fits with the highest AGN contributions to the total SED are still fairly well fit with an EAZY template, i.e., with no AGN at all. Even when an AGN is indicated, for most galaxies in the sample, the host galaxy outshines AGN emission. The fitting does not prove that our sample galaxies are Seyferts. Offering more SED templates is likely just adding more free parameters and resulting in better fits as demonstrated by the control sample, which shows a similar distribution to the CPGs in Figure 5. In fact, 86% of control-sample fits prefer an AGN-ATLAS template. Nevertheless, the fitting is consistent with the hypothesis that the morphological selection is finding AGN.

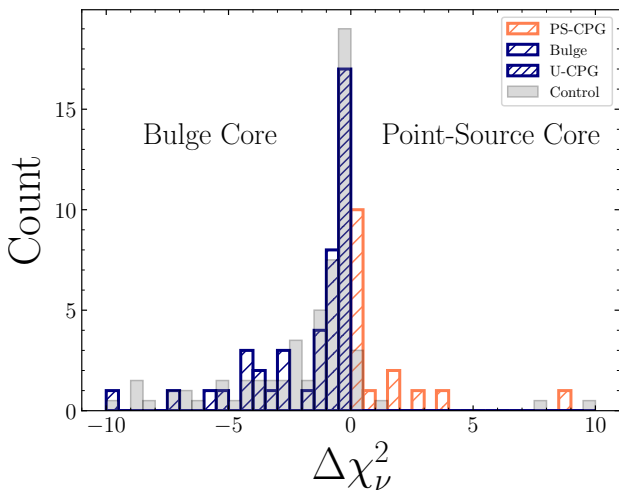


Figure 4. Histogram of the goodness of fit statistic (χ^2_ν) between the GalFit procedure that models both the CPG and control sample with a Sérsic+Sérsic two-component fit and a Sérsic+PSF two-component fit. $\Delta\chi^2_\nu \equiv \chi^2_\nu[\text{Sérsic} + \text{Sérsic}] - \chi^2_\nu[\text{Sérsic} + \text{PSF}]$, indicating a preference for a bulge core (negative values) or a point-source core (positive values). The hashed histogram identifies CPGs, with distinction being made between general CPGs (navy) and PS-CPGs (orange) to further classify and characterize the CPGs core type. The navy histogram contains hashed and double-hashed bins, identifying Bulge cores and undetermined CPGs core types, respectively. The grey histogram represents the control sample and is normalized to the CPG sample size.

3.3. SED Parameter Estimation with CIGALE

To infer the galaxies’ physical properties, we used CIGALE, an SED-fitting code relying on energy balance between the ultraviolet and infrared. The fits are good, as expected with so many free parameters, with 94% of the fits having $\chi^2_\nu \leq 1.0$. The online version of this paper includes

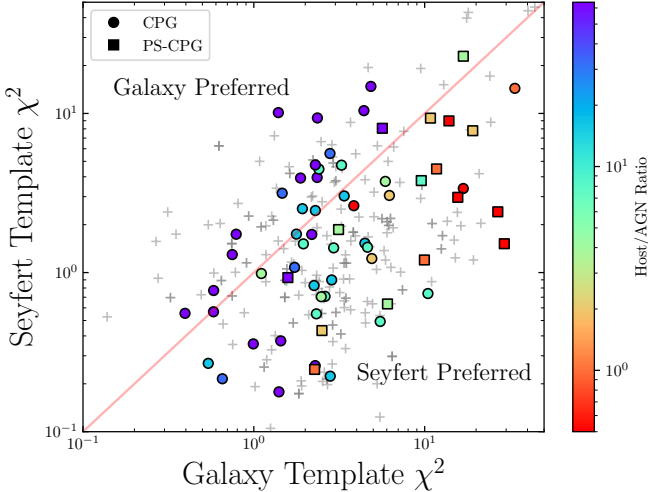


Figure 5. χ^2 of EAZY fits with and without an AGN. Colored markers represent CPGs with squares identifying PS-CPGs and circles representing the remaining CPGs. Colors indicate each CPGs’ best-fit host/AGN ratio as indicated in the color bar. Grey crosses represent control-sample galaxies. The diagonal line indicates equality, i.e., an undetermined classification. CPG IDs 1 and 29 are not plotted because their fits failed to converge owing to the core’s extreme brightness.

a Figure Set of all 66 CIGALE fits for our CPG sample, and Figure 6 shows three examples.

Fig. Set 6. CIGALE SEDs for CPGs

A CIGALE output parameter of immediate interest is f_{AGN} , the fractional contribution of AGN emission to the bolometric luminosity. We tuned CIGALE to compute f_{AGN} based on AGN emission from 0.1 to 30 μm (following Assef et al. 2013, their Eq. 1) and the NIRCam photometry.

Most interestingly, the PS-CPG median $f_{\text{AGN}} = 0.44 \pm 0.12$ while the control sample’s $f_{\text{AGN}} = 0.24 \pm 0.09$. The formal statistical separation is only at the 1σ level, though our result suggests the PS-CPG sample has measurable AGN emission in the infrared. f_{AGN} can be better constrained with additional photometry in future work, particularly in the sub-mm (see, e.g., Ciesla et al. 2015).

CIGALE also provides estimated stellar masses and star-formation rates (SFRs), which provide context for the CPGs. Typical galaxies fall on the star-formation main sequence, which depends on both redshift and stellar mass (Speagle et al. 2014, Eq. 28). As Figure 7 shows, the majority of our sample lie near the star-formation main sequence, and $\sim 31\%$ lie at or above the starburst boundary given by Rodighiero et al. (2011). An independent SFR estimate comes from radio observations (e.g., Condon 1992; Tabatabaei et al. 2017). Positions for 24 CPGs (identified in Table 1) match sources in the VLA 3 GHz catalog (Hyun et al. 2023). Generally, massive and starburst CPGs are the ones having radio detections. This could be attributed to either the synchrotron radiation

produced from remnants of Type II supernovae (e.g., Chevalier 1982), i.e., star formation, or radio emission from the AGN (e.g., Kellermann 1987), or both. Willner et al. (2023, their Fig. 11) similarly showed that few radio sources in the TDF are in the starburst range.

Figure 8 compares the inferred physical properties for the CPG and control samples. In short, the CPGs are massive galaxies with lower SFRs compared to the control sample. The PS-CPGs tend to have slightly lower inferred stellar masses and higher SFRs than other CPGs. Rosario et al. (2013) showed that AGN are more likely to be hosted by a star-forming galaxy owing to the need for cold gas to fuel both AGN and star formation, though X-ray AGN can be present in similar mass and redshift non-active galaxies. While the CPG and control samples show a similar distribution of f_{AGN} , the PS-CPGs dominate the upper quartile of CPG f_{AGN} values with $\langle f_{\text{AGN}} \rangle = 0.47$. Ciesla et al. (2015) emphasized that small f_{AGN} values from CIGALE are not well-constrained absent sub-mm photometry, and therefore the values of $f_{\text{AGN}} \lesssim 0.2$ may be overestimated. Therefore, our CIGALE inferences do not necessarily preclude AGN presence for the rest of our CPGs, though they do suggest unique AGN activity in our PS-CPGs.

Finally, CIGALE identified a visual selection bias towards massive galaxies in the CPG sample because only bright galaxies could be examined for morphology. Often it was the luminous core that qualified a galaxy for our visual sample. Regardless, PS-CPGs’ active star formation, normal stellar mass, and frequent radio loudness all suggest an AGN giving rise to a near-infrared point-source is present.

3.4. $(m_{\text{F356W}} - m_{\text{F444W}})$ Colors

Another standard AGN selection method is red ($m_{\text{F356W}} - m_{\text{F444W}}$) color (e.g., Stern et al. 2005). The NIRCam F356W and F444W filters are close to the WISE W1 and W2 filters (Wright et al. 2010) and can replicate the $(W1 - W2) > 0.80$ (Vega magnitudes) AGN color selection (e.g., Stern et al. 2012). There are 19 CPGs with $(m_{\text{F356W,Vega}} - m_{\text{F444W,Vega}}) > 0.80$ as shown in Figure 9. (Table 1 gives the CPG colors in AB-mag.) Nearly all remaining CPGs and control-sample galaxies have integrated colors consistent with a pure stellar population that formed early and evolved passively. These colors do not preclude a modest AGN or star-formation contribution, especially for higher redshift CPGs. However, PS-CPGs demonstrate a strong preference for colors consistent with an AGN (i.e., $(m_{\text{F356W}} - m_{\text{F444W}}) > 0.16$ mag), further suggesting that the near-infrared point-source feature comes from a visible AGN. This is most likely because dust obscuration decreases at the longer wavelengths (Kim et al. 2019), resulting in redder colors because an AGN is shining through the galaxy. This is consistent with the point-source feature of

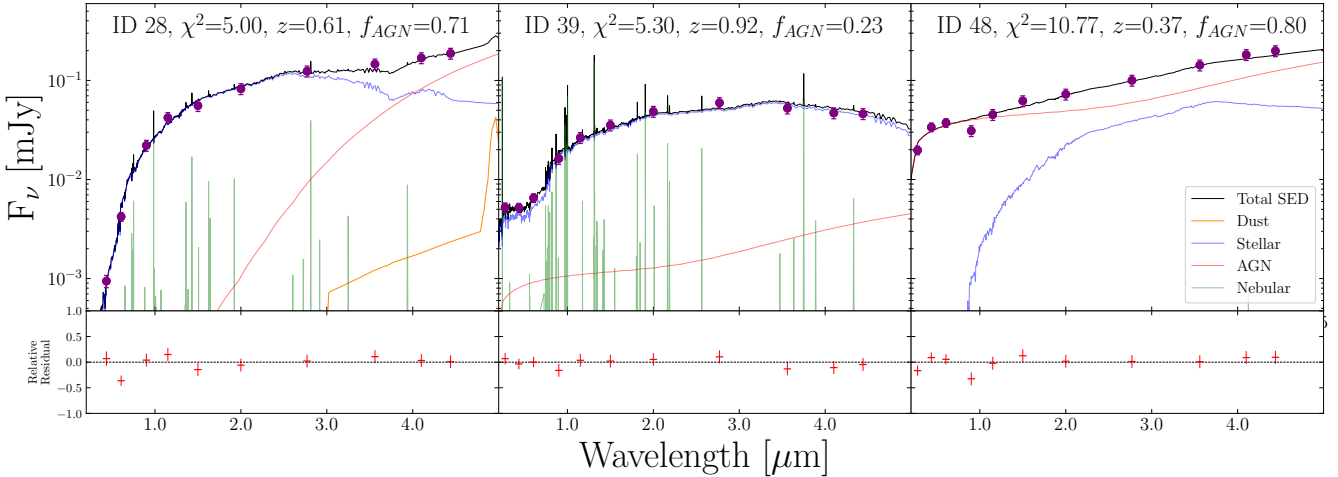


Figure 6. Example CIGALE model fits for three CPG SEDs. Fit residuals are shown below each SED panel. The CPG ID, χ^2 , photometric redshift, and f_{AGN} are indicated in each panel. The legend identifies model components included in the SED fitting. The online journal includes a figure set showing all 66 CIGALE fits.

ten dominating the reddest wavelengths of our observations (Figure 1).

4. SUMMARY & FUTURE PROSPECTS

The superb angular resolution of *JWST*/NIRCam reveals galaxies (“CPGs”) with point-like cores at the redder wavelengths. Based on *GalFit* analysis, 16/66 CPGs have a

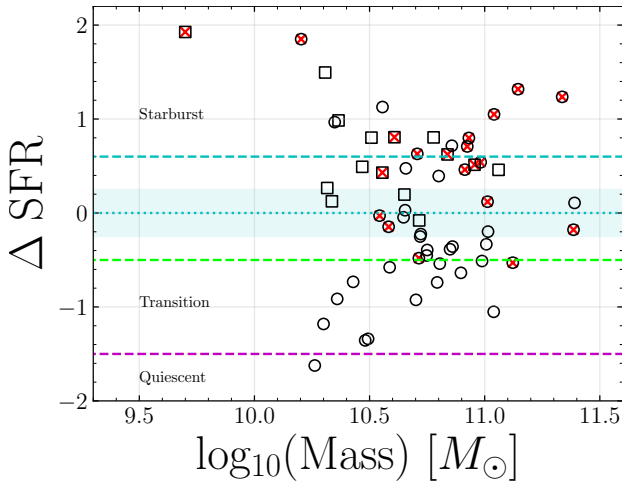


Figure 7. Star-formation rates from CIGALE relative to the respective star-formation main sequence. The y -axis shows $\Delta \text{SFR} \equiv \log_{10}(\text{SFR}) - \log_{10}(\text{SFR}_{\text{MS}})$ with SFR_{MS} defined by Speagle et al. (2014, their Eq. 28). The horizontal dotted line and shaded region mark the main sequence and the ± 0.2 dex range. The upper cyan, the middle green, and the lower magenta dashed lines mark 0.6 dex above the main sequence, commonly taken as the starburst boundary (e.g., Rodighiero et al. 2011), the lower boundary to the main sequence, and the upper boundary to the quiescent region (e.g., Renzini & Peng 2015), respectively. Circles and squares identify CPGs and PS-CPGs, respectively, and markers with ‘x’ symbols indicate sources with VLA 3 GHz matches.

point-source core. This is a much higher frequency of point-source cores than in a control sample.

Best-fit SEDs for the CPGs in the *JWST* NEP-TDF field suggest that the CPGs are massive and luminous, and in most cases, the extended galaxy outshines the unresolved core. The SEDs are well-characterized with AGN components, though the CPG sample is not AGN-dominated. However, the core classification from *GalFit* suggests that at least 14 PS-CPGs host IR-luminous AGN for the following reasons:

- 14/16 are classified as AGN via their $m_{\text{F356W}} - m_{\text{F444W}}$ colors;
- *GalFit* prefers a point-source nucleus over a compact stellar bulge in the nucleus;
- CIGALE finds $\langle f_{\text{AGN}} \rangle = 0.47$, higher than for the control sample; and
- All display the point-source signatures in their images that motivated this work (Figure 1).

Photometry at additional wavelengths and spectroscopy would aid in classifying these objects, confirming AGN presence, constraining host-galaxy parameters, and characterizing the mechanisms driving the pointlike galaxy cores for the entire CPG sample. More robust *GalFit* analysis could clarify which are either PS-CPGs or Bulge-CPGs (e.g., CPG ID 48 was classified as a Bulge-CPG despite displaying an obvious point-source signature). Additionally, cross correlation of our CPGs with X-ray detections will confirm their AGN nature and measure the nuclear luminosity and absorption. This work has identified AGN only at $4.4 \mu\text{m}$. Future work could extend this morphological classification to shorter wavelength *JWST* data to improve the angular resolution and make it more broadly applicable—despite the larger

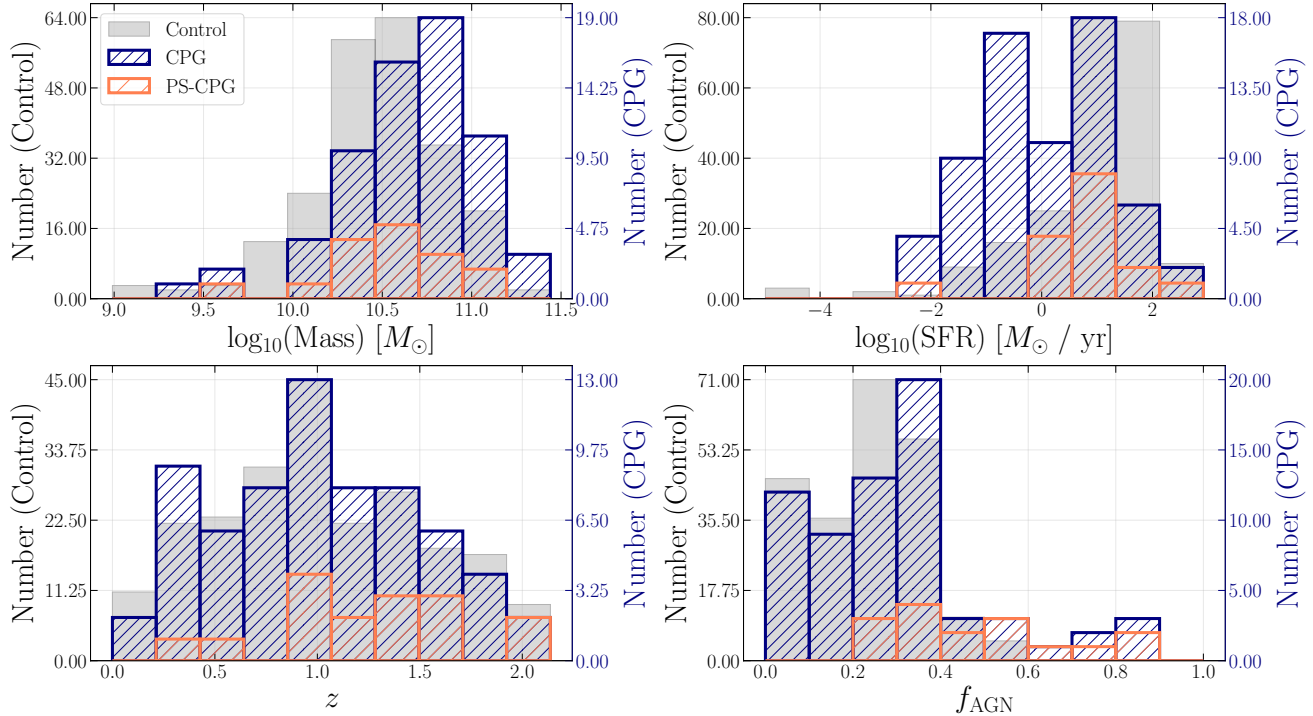


Figure 8. CIGALE-inferred physical parameters from SED fitting 0.2–4.4 μm observations. All panels are histograms of the CPG sample in navy against the control sample in gray. PS-CPGs are plotted in orange and are included in the CPG distribution. From top left, the panels show the inferred stellar mass, star-formation rates, photometric redshifts, and f_{AGN} .

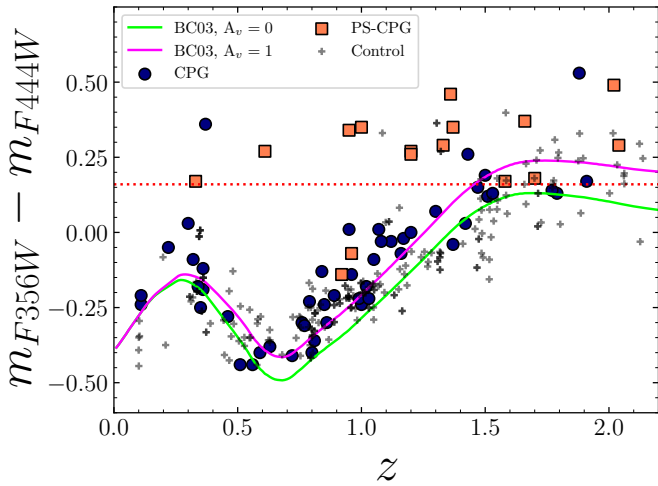


Figure 9. $(m_{\text{F356W,AB}} - m_{\text{F444W,AB}})$ color versus CIGALE-computed photometric redshift. Navy blue circles and orange squares identify CPGs and PS-CPGs, respectively. Plus signs represent galaxies in the control sample. The green and magenta lines show the colors of a galaxy that formed at $z = 5$ and has $A_V = 0$ and $A_V = 1$, respectively (Calzetti et al. 2000 extinction law). The galaxy model is a Bruzual & Charlot (2003) stellar population with Salpeter IMF, solar metallicity, and $\tau = 0.5$ Gyr exponentially declining star-formation history. The horizontal dotted line at 0.16 shows the $(m_{\text{F356W,Vega}} - m_{\text{F444W,Vega}}) = 0.8$ AGN color-selection criterion in AB mag, replicating (W1–W2) AGN colors (Assef et al. 2013).

effects from dust at the shorter wavelengths—and to test at what wavelength an automated morphological approach would break down.

The initial visual sample selection revives the classical approach to AGN identification via a bright, star-like nucleus. This simple selection method is possible because of JWST’s superb angular resolution at long wavelengths, where extinction is much lower than in visible light. Taking advantage of the near-infrared surface brightness and morphology of our CPG sample made it possible to quantify and automate the morphological approach. Future simulations and modeling can refine this procedure to constrain where the PS-CPG separation from brighter galaxies and stars can confidently exist. Even as a prototype, this automated sample selection of brighter galaxies with point-source features streamlines the search and analysis of AGN in current and future JWST/NIRCam imaging.

ROIII dedicates this work to the glory of God who makes all things possible. ROIII acknowledges support from an undergraduate Arizona NASA Space Grant, Cooperative Agreement 80NSSC20M0041. RAW, SHC, and RAJ acknowledge support from NASA JWST Interdisciplinary Scientist grants NAG5-12460, NNX14AN10G, and 80NSSC18K0200 from GSFC. This work is based on observations made with the NASA/ESA/CSA James Webb Space Telescope. The data were obtained from the Mikulski Archive for Space Telescopes (MAST) at the Space Telescope Science Institute, which is operated by the Association of Universities for Research in Astronomy, Inc., under NASA contract NAS 5-03127 for JWST. These observations are associated with JWST programs 1176, 2736, and 2738. AZ acknowledges support by Grant No. 2020750 from the United States-Israel Binational Science Foundation (BSF) and Grant No. 2109066 from the United States National Science Foundation (NSF); by the Ministry of Science & Technology, Israel; and by the Israel Science Foundation Grant No. 864/23. HBH and SNM also acknowledge support from NASA JWST Interdisciplinary Scientist grant 21-SMDSS21-0013.

All the *JWST* data used in this paper can be found in MAST: [10.17909/jtd6-af15](https://doi.org/10.17909/jtd6-af15)

Software: AstroPy (Astropy Collaboration et al. 2013, 2018, 2022); CIGALE (Boquien et al. 2019); SExtractor (Bertin & Arnouts 1996); EAZY (Brammer et al. 2008); GalFit (Peng et al. 2002); WebbPSF (Perrin et al. 2012)

Facilities: James Webb Space Telescope (*JWST*/NIRCam); Hubble Space Telescope, Very Large Array.

REFERENCES

- Antonucci, R. R. J., & Miller, J. S. 1985, ApJ, 297, 621, doi: [10.1086/163559](https://doi.org/10.1086/163559)
- Assef, R. J., Stern, D., Kochanek, C. S., et al. 2013, ApJ, 772, 26, doi: [10.1088/0004-637X/772/1/26](https://doi.org/10.1088/0004-637X/772/1/26)
- Astropy Collaboration, Robitaille, T. P., Tollerud, E. J., et al. 2013, A&A, 558, A33, doi: [10.1051/0004-6361/201322068](https://doi.org/10.1051/0004-6361/201322068)
- Astropy Collaboration, Price-Whelan, A. M., Sipőcz, B. M., et al. 2018, AJ, 156, 123, doi: [10.3847/1538-3881/aabc4f](https://doi.org/10.3847/1538-3881/aabc4f)
- Astropy Collaboration, Price-Whelan, A. M., Lim, P. L., et al. 2022, ApJ, 935, 167, doi: [10.3847/1538-4357/ac7c74](https://doi.org/10.3847/1538-4357/ac7c74)
- Bertin, E., & Arnouts, S. 1996, A&AS, 117, 393, doi: [10.1051/aas:1996164](https://doi.org/10.1051/aas:1996164)
- Bollati, F., Lupi, A., Dotti, M., & Haardt, F. 2023, On the connection between AGN radiative feedback and massive black hole spin. <https://arxiv.org/abs/2311.07576>
- Boquien, M., Burgarella, D., Roehlly, Y., et al. 2019, A&A, 622, A103, doi: [10.1051/0004-6361/201834156](https://doi.org/10.1051/0004-6361/201834156)
- Brammer, G. B., van Dokkum, P. G., & Coppi, P. 2008, ApJ, 686, 1503, doi: [10.1086/591786](https://doi.org/10.1086/591786)
- Brown, M. J. I., Duncan, K. J., Landt, H., et al. 2019, MNRAS, 489, 3351, doi: [10.1093/mnras/stz2324](https://doi.org/10.1093/mnras/stz2324)
- Bruce, V. A., Dunlop, J. S., Mortlock, A., et al. 2016, MNRAS, 458, 2391, doi: [10.1093/mnras/stw467](https://doi.org/10.1093/mnras/stw467)
- Bruzual, G., & Charlot, S. 2003, MNRAS, 344, 1000, doi: [10.1046/j.1365-8711.2003.06897.x](https://doi.org/10.1046/j.1365-8711.2003.06897.x)
- Burbidge, E. M., Burbidge, G. R., & Prendergast, K. H. 1963, ApJ, 138, 375, doi: [10.1086/147652](https://doi.org/10.1086/147652)
- Burke, C. J., Liu, X., & Shen, Y. 2024, MNRAS, 527, 5356, doi: [10.1093/mnras/stad3592](https://doi.org/10.1093/mnras/stad3592)
- Cales, S. L., & Brotherton, M. S. 2015, MNRAS, 449, 2374, doi: [10.1093/mnras/stv370](https://doi.org/10.1093/mnras/stv370)
- Calzetti, D., Armus, L., Bohlin, R. C., et al. 2000, ApJ, 533, 682, doi: [10.1086/308692](https://doi.org/10.1086/308692)
- Chevalier, R. A. 1982, ApJ, 259, 302, doi: [10.1086/160167](https://doi.org/10.1086/160167)
- Ciesla, L., Charmandaris, V., Georgakakis, A., et al. 2015, A&A, 576, A10, doi: [10.1051/0004-6361/201425252](https://doi.org/10.1051/0004-6361/201425252)
- Coe, D., Umetsu, K., Zitrin, A., et al. 2012, ApJ, 757, 22, doi: [10.1088/0004-637X/757/1/22](https://doi.org/10.1088/0004-637X/757/1/22)
- Condon, J. J. 1992, ARA&A, 30, 575, doi: [10.1146/annurev.aa.30.090192.003043](https://doi.org/10.1146/annurev.aa.30.090192.003043)
- Conselice, C. J. 2003, ApJS, 147, 1, doi: [10.1086/375001](https://doi.org/10.1086/375001)
- Costa-Souza, J. H., Riffel, R. A., Dors, O. L., Riffel, R., & da Rocha-Poppe, P. C. 2023, Spatially resolved observations of the peculiar galaxy NGC 232: AGN winds and stellar populations. <https://arxiv.org/abs/2310.15842>
- Dale, D. A., Helou, G., Magdis, G. E., et al. 2014, ApJ, 784, 83, doi: [10.1088/0004-637X/784/1/83](https://doi.org/10.1088/0004-637X/784/1/83)
- Davies, R. L., Belli, S., Park, M., et al. 2024, MNRAS, 528, 4976, doi: [10.1093/mnras/stae327](https://doi.org/10.1093/mnras/stae327)
- Elvis, M., Maccacaro, T., Wilson, A. S., et al. 1978, MNRAS, 183, 129, doi: [10.1093/mnras/183.2.129](https://doi.org/10.1093/mnras/183.2.129)

- Fanaroff, B. L., & Riley, J. M. 1974, MNRAS, 167, 31P, doi: [10.1093/mnras/167.1.31P](https://doi.org/10.1093/mnras/167.1.31P)
- Furtak, L. J., Labb  , I., Zitrin, A., et al. 2023, arXiv e-prints, arXiv:2308.05735, doi: [10.48550/arXiv.2308.05735](https://doi.org/10.48550/arXiv.2308.05735)
- Glikman, E., Lacy, M., Urrutia, T., Djorgovski, G., & Mahabal, A. 2012, in American Astronomical Society Meeting Abstracts, Vol. 219, American Astronomical Society Meeting Abstracts #219, 209.03
- Hickox, R. C., & Alexander, D. M. 2018, ARA&A, 56, 625, doi: [10.1146/annurev-astro-081817-051803](https://doi.org/10.1146/annurev-astro-081817-051803)
- Hwang, Y.-H., Wang, W.-H., Chang, Y.-Y., et al. 2021, ApJ, 913, 6, doi: [10.3847/1538-4357/abf11a](https://doi.org/10.3847/1538-4357/abf11a)
- Hyun, M., Im, M., Smail, I. R., et al. 2023, ApJS, 264, 19, doi: [10.3847/1538-4365/ac9bf4](https://doi.org/10.3847/1538-4365/ac9bf4)
- Inoue, A. K. 2011, MNRAS, 415, 2920, doi: [10.1111/j.1365-2966.2011.18906.x](https://doi.org/10.1111/j.1365-2966.2011.18906.x)
- Jansen, R. A., & Windhorst, R. A. 2018, PASP, 130, 124001, doi: [10.1088/1538-3873/aae476](https://doi.org/10.1088/1538-3873/aae476)
- Juod  balis, I., Conselice, C. J., Singh, M., et al. 2023, MNRAS, 525, 1353, doi: [10.1093/mnras/stad2396](https://doi.org/10.1093/mnras/stad2396)
- Kellermann, K. I. 1987, in Observational Evidence of Activity in Galaxies, ed. E. E. Khachikian, K. J. Fricke, & J. Melnick, Vol. 121, 273
- Kim, D., Jansen, R. A., Windhorst, R. A., Cohen, S. H., & McCabe, T. J. 2019, ApJ, 884, 21, doi: [10.3847/1538-4357/ab385c](https://doi.org/10.3847/1538-4357/ab385c)
- Li, Q., Conselice, C. J., Adams, N., et al. 2023, EPOCHS VIII. An Insight into MIRI-selected Galaxies in SMACS-0723 and the Benefits of Deep MIRI Photometry in Revealing AGN and the Dusty Universe. <https://arxiv.org/abs/2309.06932>
- Lyu, J., Alberts, S., Rieke, G. H., et al. 2023, arXiv e-prints, arXiv:2310.12330, doi: [10.48550/arXiv.2310.12330](https://doi.org/10.48550/arXiv.2310.12330)
- Mandal, A. K., Rakshit, S., Kurian, K. S., et al. 2018, MNRAS, 475, 5330, doi: [10.1093/mnras/sty200](https://doi.org/10.1093/mnras/sty200)
- Masini, A., Hickox, R. C., Carroll, C. M., et al. 2020, ApJS, 251, 2, doi: [10.3847/1538-4365/abb607](https://doi.org/10.3847/1538-4365/abb607)
- Mehdipour, M., Kriss, G. A., Kaastra, J. S., et al. 2024, ApJ, 962, 155, doi: [10.3847/1538-4357/ad1bcb](https://doi.org/10.3847/1538-4357/ad1bcb)
- O'Brien, R., Jansen, R. A., Grogin, N. A., et al. 2024, arXiv e-prints, arXiv:2401.04944, doi: [10.48550/arXiv.2401.04944](https://doi.org/10.48550/arXiv.2401.04944)
- Ohsuga, K., & Umemura, M. 2001, ApJ, 559, 157, doi: [10.1086/322398](https://doi.org/10.1086/322398)
- Oke, J. B., & Gunn, J. E. 1983, ApJ, 266, 713, doi: [10.1086/160817](https://doi.org/10.1086/160817)
- Osterbrock, D. E. 1993, RMxAA, 26, 65
- Padovani, P., Alexander, D. M., Assef, R. J., et al. 2017, A&A Rv, 25, 2, doi: [10.1007/s00159-017-0102-9](https://doi.org/10.1007/s00159-017-0102-9)
- Peng, C. Y., Ho, L. C., Impey, C. D., & Rix, H.-W. 2002, AJ, 124, 266, doi: [10.1086/340952](https://doi.org/10.1086/340952)
- Perrin, M. D., Soummer, R., Elliott, E. M., Lallo, M. D., & Sivaramakrishnan, A. 2012, in Society of Photo-Optical Instrumentation Engineers (SPIE) Conference Series, Vol. 8442, Space Telescopes and Instrumentation 2012: Optical, Infrared, and Millimeter Wave, ed. M. C. Clampin, G. G. Fazio, H. A. MacEwen, & J. Oschmann, Jacobus M., 84423D, doi: [10.1117/12.925230](https://doi.org/10.1117/12.925230)
- Planck Collaboration, Ade, P. A. R., Aghanim, N., et al. 2016, A&A, 594, A13, doi: [10.1051/0004-6361/201525830](https://doi.org/10.1051/0004-6361/201525830)
- Planck Collaboration, Aghanim, N., Akrami, Y., et al. 2020, A&A, 641, A6, doi: [10.1051/0004-6361/201833910](https://doi.org/10.1051/0004-6361/201833910)
- Poulasis, E., Georgantopoulos, I., Bonanos, A. Z., et al. 2019, MNRAS, 487, 4285, doi: [10.1093/mnras/stz1483](https://doi.org/10.1093/mnras/stz1483)
- Renzini, A., & Peng, Y.-j. 2015, ApJL, 801, L29, doi: [10.1088/2041-8205/801/2/L29](https://doi.org/10.1088/2041-8205/801/2/L29)
- Richards, G. T., Hall, P. B., Vanden Berk, D. E., et al. 2003, AJ, 126, 1131, doi: [10.1086/377014](https://doi.org/10.1086/377014)
- Rigby, J., Perrin, M., McElwain, M., et al. 2023, PASP, 135, 048001, doi: [10.1088/1538-3873/acb293](https://doi.org/10.1088/1538-3873/acb293)
- Robotham, A. S. G., D'Silva, J. C. J., Windhorst, R. A., et al. 2023, PASP, 135, 085003, doi: [10.1088/1538-3873/acea42](https://doi.org/10.1088/1538-3873/acea42)
- Robotham, A. S. G., Taranu, D. S., Tobar, R., Moffett, A., & Driver, S. P. 2017, MNRAS, 466, 1513, doi: [10.1093/mnras/stw3039](https://doi.org/10.1093/mnras/stw3039)
- Rodighiero, G., Daddi, E., Baronchelli, I., et al. 2011, ApJL, 739, L40, doi: [10.1088/2041-8205/739/2/L40](https://doi.org/10.1088/2041-8205/739/2/L40)
- Rosario, D. J., Santini, P., Lutz, D., et al. 2013, ApJ, 771, 63, doi: [10.1088/0004-637X/771/1/63](https://doi.org/10.1088/0004-637X/771/1/63)
- Rutkowski, M. J., Hegel, P. R., Kim, H., Tamura, K., & Windhorst, R. A. 2013, Astron. J., 146, 11, doi: [10.1088/0004-6256/146/1/11](https://doi.org/10.1088/0004-6256/146/1/11)
- Sampaio, V. M., Arag  n-Salamanca, A., Merrifield, M. R., et al. 2023, MNRAS, 524, 5327, doi: [10.1093/mnras/stad2211](https://doi.org/10.1093/mnras/stad2211)
- Seyfert, C. K. 1943, ApJ, 97, 28, doi: [10.1086/144488](https://doi.org/10.1086/144488)
- Speagle, J. S., Steinhardt, C. L., Capak, P. L., & Silverman, J. D. 2014, ApJS, 214, 15, doi: [10.1088/0067-0049/214/2/15](https://doi.org/10.1088/0067-0049/214/2/15)
- Stalevski, M., Ricci, C., Ueda, Y., et al. 2016, MNRAS, 458, 2288, doi: [10.1093/mnras/stw444](https://doi.org/10.1093/mnras/stw444)
- Stern, D., Eisenhardt, P., Gorjian, V., et al. 2005, ApJ, 631, 163, doi: [10.1086/432523](https://doi.org/10.1086/432523)
- Stern, D., Assef, R. J., Benford, D. J., et al. 2012, ApJ, 753, 30, doi: [10.1088/0004-637X/753/1/30](https://doi.org/10.1088/0004-637X/753/1/30)
- Tabatabaei, F. S., Schinnerer, E., Krause, M., et al. 2017, ApJ, 836, 185, doi: [10.3847/1538-4357/836/2/185](https://doi.org/10.3847/1538-4357/836/2/185)
- Trump, J. R., Hsu, A. D., Fang, J. J., et al. 2013, ApJ, 763, 133, doi: [10.1088/0004-637X/763/2/133](https://doi.org/10.1088/0004-637X/763/2/133)
- Wang, J., Xu, D. W., Wang, Y., et al. 2019, ApJ, 887, 15, doi: [10.3847/1538-4357/ab4d90](https://doi.org/10.3847/1538-4357/ab4d90)
- Wilkes, B. J., Schmidt, G. D., Cutri, R. M., et al. 2002, ApJL, 564, L65, doi: [10.1086/338908](https://doi.org/10.1086/338908)

- Willner, S. P., Gim, H. B., del Carmen Polletta, M., et al. 2023, ApJ, 958, 176, doi: [10.3847/1538-4357/acdfb](https://doi.org/10.3847/1538-4357/acdfb)
- Windhorst, R. A., & Cohen, S. H. 2010, in American Institute of Physics Conference Series, Vol. 1294, First Stars and Galaxies: Challenges for the Next Decade, ed. D. J. Whalen, V. Bromm, & N. Yoshida (AIP), 225–233, doi: [10.1063/1.3518858](https://doi.org/10.1063/1.3518858)
- Windhorst, R. A., Cohen, S. H., Jansen, R. A., et al. 2023, AJ, 165, 13, doi: [10.3847/1538-3881/aca163](https://doi.org/10.3847/1538-3881/aca163)
- Wright, E. L., Eisenhardt, P. R. M., Mainzer, A. K., et al. 2010, AJ, 140, 1868, doi: [10.1088/0004-6256/140/6/1868](https://doi.org/10.1088/0004-6256/140/6/1868)
- Yang, G., Caputi, K. I., Papovich, C., et al. 2023, ApJL, 950, L5, doi: [10.3847/2041-8213/acd639](https://doi.org/10.3847/2041-8213/acd639)
- York, D. G., Adelman, J., Anderson, John E., J., et al. 2000, AJ, 120, 1579, doi: [10.1086/301513](https://doi.org/10.1086/301513)
- Zhao, X., Civano, F., Fornasini, F. M., et al. 2021, MNRAS, 508, 5176, doi: [10.1093/mnras/stab2885](https://doi.org/10.1093/mnras/stab2885)

Table 1 (continued)

ID	R.A.	Decl.	F275W	F435W	F606W	F090W	F115W	F150W	F200W	F277W	F356W	F410M	F444W	z	f_{AGN}	color	H23
	J2000	J2000	AB mag												AB mag		
(1)	(2)	(3)	(4)	(5)	(6)	(7)	(8)	(9)	(10)	(11)	(12)	(13)	(14)	(15)	(16)	(17)	(18)
54	260.701071	+65.876123	...	25.98	23.78	21.86	21.33	20.93	20.62	20.39	20.61	20.94	21.05	0.56	0.07	-0.44	...
55	260.73803	+65.9028757	...	27.06	26.17	24.04	22.76	22.16	21.71	21.23	20.97	20.73	20.51	1.36	0.66	0.46	...
56	260.708784	+65.876954	26.69	...	25.62	24.01	22.44	21.85	21.55	21.26	21.15	21.1	21.02	1.79	0.36	0.13	...
57	260.651265	+65.8935901	27.95	27.81	25.81	23.5	22.6	22.07	21.68	21.37	21.24	21.27	21.33	1.05	0.34	-0.09	...
58	260.668029	+65.8778179	24.97	27.77	25.18	23.65	22.46	21.76	21.16	20.62	20.29	20.15	20.03	1.43	0.4	0.26	187
59	260.665718	+65.8772567	25.42	27.52	26.35	24.78	23.24	22.31	21.92	21.59	21.42	21.32	21.25	1.91	0.38	0.17	...
60	260.690274	+65.8996399	22.37	21.4	20.99	20.67	20.29	20.24	20.23	20.28	1.37	0.3	-0.04	...
61	260.668589	+65.8807234	25.36	23.86	23.31	21.78	21.16	20.74	20.43	20.04	19.88	19.83	19.87	0.95	0.28	0.01	...
62	260.709682	+65.8805701	25.76	25.99	25.45	24.22	23.03	22.44	21.95	21.43	21.23	21.05	21.04	1.5	0.33	0.19	...
63	260.62903	+65.8741014	...	25.8	25.72	24.68	23.15	22.42	21.91	21.4	21.17	21.0	21.03	1.77	0.32	0.14	...
64	260.649498	+65.8709509	26.83	24.95	24.46	22.85	21.98	21.72	21.58	21.39	21.21	21.02	20.95	1.2	0.44	0.26	...
65	260.739964	+65.9251014	25.13	24.63	23.57	21.89	21.15	20.62	20.04	19.59	19.68	19.93	19.99	0.77	0.11	-0.31	292
66	260.672783	+65.9111158	24.73	23.24	22.45	21.93	21.51	21.38	21.29	21.2	1.7	0.37	0.18	...

NOTE—Columns show ID number, J2000 positions, AB mag in three *HST* filters and eight *JWST*/NIRCam filters, photometric redshift (z) as measured by CIGALE, f_{AGN} from CIGALE, $(m_{\text{F356W}} - m_{\text{F444W}})$ color, and counterpart ID in the Hyun et al. (2023) (H23) VLA 3 GHz source catalog. The CIGALE fits incorporated a stellar continuum component from Bruzual & Charlot (2003) models, a dust component from Dale et al. (2014) templates, a Calzetti et al. (2000) dust attenuation law, nebular emission templates from Inoue (2011), and a clumpy two-phase torus model from Stalevski et al. (2016).

Table 2. Catalog of GalFit output parameters for two-component fitting of our visual sample.

ID	Sérsic + Sérsic						χ^2_ν	Sérsic + PSF						Core Type
	mag	R_e	n	mag	R_e	n		mag	R_e	n	mag	χ^2_ν		
	Sérsic 1			Sérsic 2				Sérsic 1			PSF 1			
(1)	(2)	(3)	(4)	(5)	(6)	(7)	(8)	(9)	(10)	(11)	(12)	(13)	(14)	
1	16.52	4.00	6.00	16.52	25.00	6.00	109.26	17.68	30.00	2.21	20.68	185.59		Bulge
2	21.02	4.00	1.11	21.02	4.00	6.00	1.57	20.41	4.00	2.25	22.80	1.51		Point-Source
3	20.34	5.66	3.05	20.34	16.28	0.83	2.06	19.79	10.94	1.96	22.79	3.12		Bulge
4	20.97	4.00	3.95	20.97	16.05	3.65	1.93	19.68	11.88	4.01	22.68	2.22		Undetermined
5	20.80	6.20	0.74	20.80	7.63	4.74	1.87	20.15	5.25	2.56	23.15	5.82		Bulge
6	20.46	4.00	2.29	20.46	4.00	1.95	3.65	19.91	4.00	1.87	22.79	3.45		Point-Source
7	20.83	4.00	6.00	20.83	4.00	0.99	8.06	20.49	4.00	1.31	21.59	5.32		Point-Source
8	20.19	23.88	0.77	20.19	4.00	1.04	1.72	19.53	11.04	3.07	22.53	4.77		Bulge
9	21.21	4.00	1.59	21.21	4.00	6.00	3.01	21.07	4.00	1.47	22.72	2.68		Point-Source
10	21.36	4.00	1.29	21.36	4.00	4.71	1.53	20.83	4.00	1.86	23.33	1.31		Point-Source
11	20.92	4.00	2.66	20.92	4.41	6.00	1.86	20.36	4.00	4.08	23.36	2.07		Undetermined
12	21.77	16.92	0.70	21.77	4.05	1.76	1.47	20.59	6.71	2.81	23.59	2.28		Bulge
13	21.33	12.39	4.04	21.33	4.00	1.25	1.12	20.54	4.42	2.86	23.54	1.51		Undetermined
14	20.49	4.00	6.00	20.49	4.00	0.89	9.08	20.34	4.00	1.09	20.72	5.27		Point-Source
15	18.88	24.11	1.12	18.88	4.00	0.70	20.71	18.61	18.97	2.26	21.45	25.07		Bulge

Table 2 continued

Table 2 (continued)

ID	Sérsic + Sérsic							Sérsic + PSF							Core Type
	Sérsic 1			Sérsic 2			χ^2_ν	Sérsic 1			PSF 1				
	mag	R _e	n	mag	R _e	n		mag	R _e	n	mag	χ^2_ν	(14)		
(1)	(2)	(3)	(4)	(5)	(6)	(7)	(8)	(9)	(10)	(11)	(12)	(13)	(14)		
16	19.00	6.61	0.70	19.00	18.44	2.37	12.37	18.36	7.21	3.43	21.36	93.77		Bulge	
17	18.86	15.75	3.64	18.86	4.00	2.06	3.99	18.78	10.15	4.45	21.78	13.56		Bulge	
18	22.53	4.00	0.70	22.53	10.02	1.75	1.84	20.69	8.37	2.08	23.69	2.27		Undetermined	
19	21.17	7.42	1.23	21.17	4.00	6.00	1.09	20.91	6.57	1.73	23.91	1.16		Undetermined	
20	19.64	12.88	5.65	19.64	25.00	6.00	16.59	19.16	17.39	5.44	22.16	35.62		Bulge	
21	23.06	4.00	0.85	23.06	8.98	2.14	1.14	20.59	8.68	1.85	23.59	1.18		Undetermined	
22	21.53	23.52	6.00	21.53	4.25	2.54	1.75	20.62	5.11	3.05	23.62	2.23		Undetermined	
23	21.55	15.25	1.29	21.55	4.00	2.74	2.18	20.31	5.72	2.63	23.31	2.91		Bulge	
24	20.87	14.47	6.00	20.87	5.66	2.08	1.61	19.92	5.94	2.69	22.92	2.96		Bulge	
25	21.38	4.00	6.00	21.38	4.00	6.00	4.58	21.13	4.00	6.00	22.10	2.67		Point-Source	
26	21.42	28.29	0.70	21.42	11.88	3.56	18.16	19.53	14.50	2.52	22.53	19.77		Bulge	
27	20.23	8.61	0.70	20.23	7.46	0.70	8.42	19.85	8.16	0.70	22.85	11.20		Bulge	
28	18.83	4.00	3.51	18.83	4.00	6.00	55.99	18.53	4.00	4.61	19.94	47.26		Point-Source	
29	20.02	25.01	5.32	20.02	9.24	2.84	1.98	19.61	10.83	3.04	22.61	5.51		Bulge	
30	22.37	30.00	6.00	22.37	4.00	6.00	3.58	21.87	4.00	6.00	24.33	1.81		Point-Source	
31	21.87	8.48	6.00	21.87	16.45	4.41	3.45	19.40	13.62	3.15	22.40	8.98		Bulge	
32	21.82	4.00	6.00	21.82	4.00	1.08	1.35	21.23	4.00	1.51	22.89	1.38		Undetermined	
33	21.23	4.00	6.00	21.23	4.00	1.71	4.20	20.34	4.00	2.89	23.14	4.74		Bulge	
34	20.62	8.30	1.37	20.62	4.00	1.96	1.87	20.05	6.54	1.56	23.05	2.26		Undetermined	
35	21.58	4.00	6.00	21.58	4.00	6.00	2.21	20.43	4.00	6.00	23.36	1.86		Point-Source	
36	20.90	4.09	2.18	20.90	12.93	0.70	1.38	20.40	7.94	1.62	23.40	1.98		Bulge	
37	21.20	15.53	0.70	21.20	8.04	4.29	1.95	19.50	9.69	2.38	22.50	2.95		Bulge	
38	20.23	6.44	6.00	20.23	4.00	6.00	3.18	19.67	5.48	6.00	22.41	3.01		Point-Source	
39	20.12	4.00	4.67	20.12	4.00	6.00	7.25	19.77	4.00	4.33	22.60	6.88		Point-Source	
40	21.17	5.26	1.88	21.17	7.63	3.53	1.06	20.69	6.11	2.07	23.69	1.21		Undetermined	
41	20.89	5.45	1.44	20.89	25.00	6.00	5.83	20.77	4.66	2.20	23.77	8.68		Bulge	
42	21.48	4.00	3.76	21.48	4.00	6.00	1.62	20.68	4.00	3.95	23.20	1.37		Point-Source	
43	19.18	30.00	3.03	19.18	4.00	0.79	4.60	19.00	10.64	5.95	22.00	18.97		Bulge	
44	21.43	16.03	0.70	21.43	4.00	2.40	1.23	20.53	8.94	2.26	23.49	1.75		Bulge	
45	18.94	10.41	4.57	18.94	25.00	0.70	9.74	18.97	12.67	2.71	21.97	14.97		Bulge	
46	20.18	5.41	2.09	20.18	25.00	6.00	17.06	19.74	7.16	2.65	22.74	18.40		Bulge	
47	20.02	4.00	0.72	20.02	25.00	0.70	4.56	19.51	8.61	3.02	22.51	15.58		Bulge	
48	20.29	25.12	0.70	20.29	4.00	6.00	13.22	18.51	9.80	3.64	19.44	17.46		Bulge	
49	19.97	30.00	6.00	19.97	7.14	2.63	3.54	19.72	9.36	3.44	22.72	6.11		Bulge	
50	20.31	6.99	2.59	20.31	5.79	3.55	1.26	20.16	7.40	2.16	23.16	1.53		Undetermined	
51	20.23	5.27	0.87	20.23	25.00	2.28	31.77	18.41	19.72	2.32	21.41	60.68		Bulge	
52	19.69	7.67	5.57	19.69	15.23	0.70	41.44	18.87	13.86	0.72	21.04	45.58		Bulge	
53	21.26	25.59	0.70	21.26	4.00	6.00	36.44	19.29	9.68	2.85	20.20	48.88		Bulge	

Table 2 continued

Table 2 (*continued*)

ID	Sérsic + Sérsic							Sérsic + PSF							Core Type	
	Sérsic 1			Sérsic 2				χ^2_ν	Sérsic 1			PSF 1				
	mag	R_e	n	mag	R_e	n	(8)		(9)	(10)	(11)	mag	R_e	n	(12)	(14)
(1)	(2)	(3)	(4)	(5)	(6)	(7)	(8)		(9)	(10)	(11)	(12)	(13)			
54	21.49	4.00	2.27	21.49	4.55	4.61	0.87	21.01	4.32	2.54	24.01	1.01			Undetermined	
55	21.34	4.00	2.87	21.34	4.00	4.28	2.68	20.81	4.00	1.68	21.84	1.83			Point-Source	
56	21.93	6.44	3.60	21.93	4.00	2.13	1.04	21.02	4.37	2.05	24.02	1.08			Undetermined	
57	22.03	6.92	6.00	22.03	4.00	1.39	1.12	21.36	4.00	3.01	24.36	1.34			Undetermined	
58	20.68	8.08	0.70	20.68	6.17	2.97	2.23	20.07	7.39	1.06	23.07	3.29			Bulge	
59	21.93	4.00	6.00	21.93	4.00	0.84	1.95	21.26	4.00	2.87	23.71	2.58			Bulge	
60	20.36	5.24	3.39	20.36	11.66	0.70	1.23	20.27	6.74	2.34	23.27	1.38			Undetermined	
61	20.44	15.60	0.70	20.44	4.94	1.31	7.62	19.91	10.78	1.59	22.54	14.69			Bulge	
62	21.81	4.00	6.00	21.81	4.00	0.89	1.06	21.03	4.00	1.58	23.98	1.27			Undetermined	
63	21.80	9.66	6.00	21.80	4.00	2.85	1.49	21.06	4.51	3.42	24.06	1.60			Undetermined	
64	21.93	4.00	6.00	21.93	4.00	2.15	4.23	21.08	4.00	2.32	22.84	3.95			Point-Source	
65	20.17	11.32	1.78	20.17	12.22	1.73	2.94	20.02	12.41	1.28	23.02	3.55			Bulge	
66	21.24	4.00	1.74	21.24	4.00	6.00	1.40	21.25	4.00	1.60	23.95	1.35			Point-Source	

NOTE—Columns show ID number, AB mag, half-light radius, Sérsic index, and χ^2_ν for respective components in two-component fits with GalFit. The galaxy core-type classification is the final column, which is determined by which fit—double-Sérsic or Sérsic + PSF—has χ^2_ν closest to 1. Constraints on GalFit parameters are as follows for each two-component fit: Sérsic+Sérsic: $\text{mag} \pm 3$ of MAG_AUTO_{F444W} (via SExtractor), $0.7 \leq n \leq 6.0$, $R_e \geq 4$ pixels ($=0''.12$). Sérsic+PSF: $\text{mag}_{\text{Sérsic}} \pm 3$ of MAG_AUTO_{F444W} (via SExtractor), $\frac{1}{3} \leq \frac{\text{mag}_{\text{Sérsic}}}{\text{mag}_{\text{PSF}}} \leq 3$, $0.7 \leq n \leq 6.0$, $R_e \geq 4$ pixels ($=0''.12$).